Changes in surge and pitch decay periods of floating wind turbines for varying wind speed.

Carlos Eduardo S. Souza, Erin E. Bachynski

Abstract

Recently published experimental results show variations in surge and pitch decay periods of floating wind turbines (FWTs) subjected to different incident wind velocities. This paper explores the external loads acting on a FWT, with special attention to nonlinearities which affect its low-frequency global motions. The period variations in surge and pitch are found to have different sources. In surge, the mooring system nonlinearities dominate, while for pitch the relative phase between the nacelle velocity and the thrust induced in the rotor leads to an "apparent inertia/damping" effect. Simplified 2-DOF models using linearized stiffness coefficients for surge and modified inertia and damping matrices for pitch are developed. Comparisons with state-of-the-art aero-hydro-servo-elastic time-domain simulations show excellent agreement for three distinct catenary-moored FWT designs.

Keywords: Floating wind turbines, mooring systems, coupled dynamics

1. Introduction

Floating wind turbines (FWTs) have been proposed as the next generation of offshore wind energy harvesting systems. Some prototypes have already been deployed with power varying between 2-6 MW [1–3], while the generous wind resources at deeper waters and the more relaxed constraints in tower and rotor dimensions have resulted in ambitious concepts for supporting 10 MW turbines [4, 5]. Still, several challenges are to be overcome before FWTs become technically and commercially feasible. In particular, the platform construction costs have to be reduced.

A good understanding of FWT dynamics is necessary for optimal structural design and accurate power production estimates. However, FWTs are complex systems, subjected to nonlinear, coupled aerodynamic, hydrodynamic, mooring and controller-induced loads. Prediction of the system responses to different environmental conditions may be complicated, and unexpected behavior may be observed depending on the combination of loads.

One such behavior has been recently observed in FWT model tests, first reported in [6]. The natural periods measured in surge and pitch decay tests varied when a scale-model FWT was subjected to different incident wind velocities. The effect was noticed in both the below- and above-rated wind velocity regimes. Another model test campaign [7] reported the same phenomenon, but the tests were limited to pitch decay in above-rated wind velocities. The authors propose a qualitative explanation for the effect based on Taylor expansion of the thrust, considering the blade-pitch control action, but do not provide a prediction for the changes – nor do they discuss the effect for surge motions. In both publications, the model FWTs corresponded to catenary-moored semi-submersible platforms.

Low-frequency motions are of great importance in the design of a FWT. The low-frequency components of the aerodynamic thrust, second-order wave loads and the mooring system loads may excite rigid-body responses. The observed variations in natural period are therefore particularly important for the mooring system design and tuning of rotor controller gains.

In addition, there is a growing interest in the development of simplified models (e.g. frequency-domain approaches) that can reproduce FWT dynamics with an acceptable level of accuracy, for efficient application in early design iterations [8, 9]. An accurate estimation of the decay periods for different operational conditions is necessary for proper tuning of such models, ensuring a fair prediction of the rigid-body response to linear loads.

1.1. Background

Previous expertise and tools from the offshore industry have been adapted for the analysis of FWTs dynamics – in particular, the technology and software for platform structural analysis, wave-structure interaction and mooring system design. Ormberg & Larsen [10] introduced a method for simultaneously evaluating the floater motions and FEM-modeled mooring dynamics of a floating platform, in time-domain. The model was later updated [11, 12] for inclusion of flexible tower and blades, and wind turbine aerodynamics and control. A different approach was taken by Jonkman [13], who extended a land-based wind turbine analysis software for applications with floating substructures. The hydrodynamics and mooring models were nevertheless also borrowed from established knowledge of offshore engineering disciplines.

Brown [14] summarizes the fundamental theory and practical design aspects of catenary mooring systems, highlighting the intrinsic nonlinear relation between platform excursion and the horizontal restoring component. Mooring systems for FWTs normally consist of 3-4 lines, which may combine chain and polyester segments. For simulation purposes, it may be convenient to assume simpler configurations with a uniform cross-section [15–17].

Wind turbine aerodynamics can be reproduced with fairly simple models, like the Blade Element Momentum (BEM) method which is based on the equilibrium between aerodynamic loads on elements of the blade and the changes in fluid momentum through the rotor plane [18]. Corrections for large induction factors and tip/hub losses, respectively, are normally considered with simple multipliers, and additional accuracy may be obtained by adopting Øye's models for dynamic stall and dynamic wake effects [19]. Though developed for ground-fixed wind turbines, these models are also suitable for FWTs, especially in terms of thrust prediction [20]. Pedersen [21] proposed a different approach for finding thrust and torque, based on circulation theory, arriving to a convenient model where the interconnected nature of both loads becomes evident through a compact matrix representation.

A wind turbine model comprises the main aerodynamic characteristics of the blades (i.e., lift/drag coefficients and geometric parameters); rotor and drivetrain mechanical properties; and control system strategies and parameters. The NREL 5 MW reference wind turbine [22] provides realistic parameters for the turbine subsystems. A *Variable Speed Variable Pitch* (VSVP) control system is adopted, actuating both on the generator torque and on the collective-blade pitch angle in order to regulate

power production under different operating regimes.

The adoption of a blade-pitch controller for FWTs results in the instabilities reported in e.g. [23–25], leading to amplification of the platform surge and pitch motions. This effect may be attenuated by proper detuning of the controller gains, by placing the controller frequency away from the FWT surge/pitch natural rigid-body modes.

1.2. Scope and text organization

This paper explores the phenomenon of surge and pitch decay period variation when the FWT is subjected to different incident wind velocities. In Section 2, three different platform concepts are considered. Surge and pitch decay simulations are performed for each, under steady incident wind velocities covering the entire operational range, and the period variations are highlighted. Section 3 discusses FWT dynamics and introduces a simplified 2-DOF model to be used in the prediction of the periods. In Section 4, the period variation is related to the mooring system nonlinearities and to an "apparent" inertia and damping effect, and a strategy to consider these effects in the simplified model is developed. The predicted periods are compared with the simulations in Section 5, and conclusions and final considerations are presented in Section 6.

2. The decay period changing phenomenon

In order to illustrate the effect of changing surge/pitch decay periods for FWTs under varying incident velocities, time-domain simulations with three platform concepts are presented.

2.1. FWT concepts considered

The FWT models considered have all been published previously, and support the NREL 5 MW wind turbine [22]. The platforms and mooring systems are briefly described below:

OC3-Hywind [15] A spar platform originally developed by the Norwegian company Equinor (formerly Statoil) and adapted as a concept design for the Offshore Code Comparison Collaboration (OC3). The mooring system is composed of 3 catenary homogeneous lines, with one of them aligned with the positive x-axis and forming an angle of 120°with the other two.

OC4semi [16] A semi-submersible platform, comprising a central column connected through thin braces to three side columns. At the bottom of each column there is a "heave column", that is, a segment with larger diameter with the purpose of increasing the heave added mass and damping. The mooring system is also a 3-lines catenary configuration, but with two lines in the fore and another aligned with the negative x-axis.

CSC5MW [17, 26] Another semi-submersible platform, differing from the former in that the three side columns are connected to the central column with pontoons, instead of braces. The pontoons contribute significantly to the buoyancy and are symmetrically distributed. The mooring system also consists of three homogeneous catenary lines, arranged similarly to the OC3Hywind.

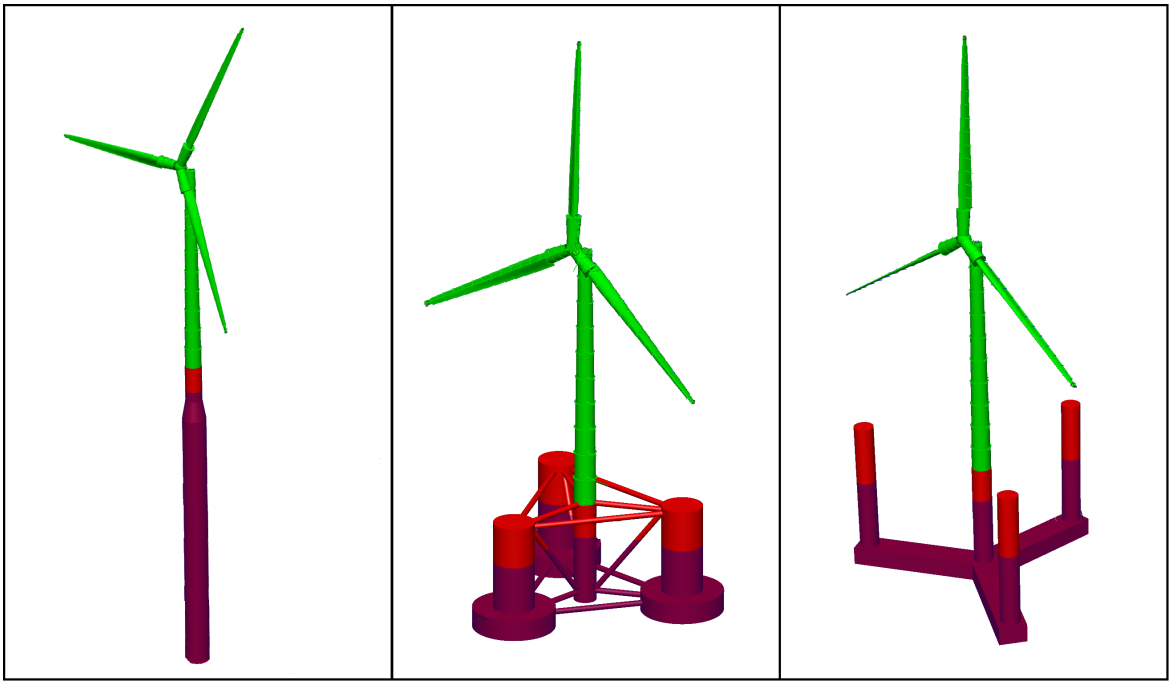

Figure 1: FWT concepts considered in the simulations. From left to right: OC3-Hywind, OC4semi and CSC5MW.

Table 1: FWTs' main properties. Δ is the displacement, I_{yy} is the moment of inertia around a transversal axis at still water level (SWL), D is the draft, z_{CG} is the vertical coordinate of the center of gravity with respect to the SWL, z_{fl} is the vertical position of the mooring lines fairleads and d_w is the water depth.

	Δ (10^3 kg)	I_{yy} (10^6 kg.m^2)	D (m)	z_{CG} (m)	z_{fl} (m)	d_w (m)
OC3-Hywind	8066.0	68017.7	120.0	-77.99	-70.0	320.0
OC4semi	14069.7	12692.7	20.0	-9.88	-14.0	200.0
CSC5MW	10215.7	13807.7	30.0	-18.92	-27.0	200.0

Figure 1 shows the three FWT concepts, and Table 1 presents their main dimensions. The tower model has also been obtained from [22], and consists of a 77.6 m long tubular structure, with a base diameter of 6.50 m and top diameter of 3.87 m. The tower base lies at 10.0 m above SWL on all platforms, such that the top is 87.6 m high. The resulting hub height is 90.0 m.

2.2. Simulation tool and procedure

The decay simulations are carried out with SIMA, which combines RIFLEX [27] and SIMO [28] in coupled time-domain simulations[1]. SIMO is a simulator of marine operations, and is responsible for computing the hydrodynamic loads on the platform. RIFLEX is a FEM based software for analysis of slender marine structures, and is used for the analysis of structural loads and displacements of the

[1]The adopted simulation tool has been compared to other codes and experimental results. For example, decay simulations results (without wind) had excellent agreement with similar software in the context of OC3 [29] and OC4 [30]. The aerodynamic module was compared with other codes and experimental results within OC5 [31], also providing very satisfactory matching with the results obtained by the other participants.

Table 2: Wind velocities considered for the decay simulations.

U_w (m/s)								
0.0	3.0	4.0	5.0	6.0	7.0	8.0	9.0	10.0
11.0	11.4	12.0	13.0	14.0	15.0	16.0	17.0	18.0
19.0	20.0	21.0	22.0	23.0	24.0	25.0		

tower, rotor blades (beam elements) and mooring lines (bar elements). In addition, it calculates the aerodynamic loads, based on the BEM method [18] with corrections for dynamic wake and dynamic stall effects; and rotor dynamics, including control.

Structural damping is included in the FE model by means of Rayleigh damping. Since moored floating platforms have compliant low-frequency modes, only the stiffness-proportional term is considered [32]. Then, the damping model attenuates higher frequency structural vibrations and numerical noise, while the platform motions are damped by hydrodynamic and aerodynamic effects only.

The simulations consisted in applying an initial displacement in the positive x direction, for the decay in surge, or a positive angle θ, for the decay in pitch. The platform was then released to oscillate, under the action of the rotor thrust. It is noted that the initial displacements were applied in addition to the loads imposed by the incident wind – i.e., the platforms oscillated around the static displacements caused by the thrust.

Surge and pitch decay tests were simulated for each of the wind velocities (U_w) of Table 2, which cover the entire operational range of the NREL 5 MW wind turbine (in addition to the free decay condition, i.e., $U_w = 0$).

2.3. Decay simulation results

For each simulation, the decay period was determined as the average period between oscillation peaks, using the statistical tool WAFO [33]. For wind velocities near rated, the limit-cycle behaviour arising from the control-induced negative damping effect [23, 25] is noticed, as illustrated in Figure 2. It is then important to constrain the analysis to a limited time window after the platform is released, in order to ensure that the cycles considered for the period measurement are dominated by the decay motion. Nonetheless, the measured periods close to rated wind velocity are expected to be less accurate than those for which the limit-cycle effect is minor or non-existent.

The decay periods for surge and pitch as a function of incident wind velocity are shown in Figure 3. For the surge decay periods (left-hand column), the pattern is similar for both the OC3-Hywind and the CSC5MW concepts: the period increases in the below-rated region, reaching a maximum at the rated wind speed (U_w = 11.4 m/s); and then decreases slowly for increasing velocities in the above-rated region, but always lying above the free-decay[2] period. For the OC4semi concept, however, the pattern is somewhat the opposite: the period decreases for increasing velocities in the

[2]I.e., the decay for $U_w = 0$ m/s.

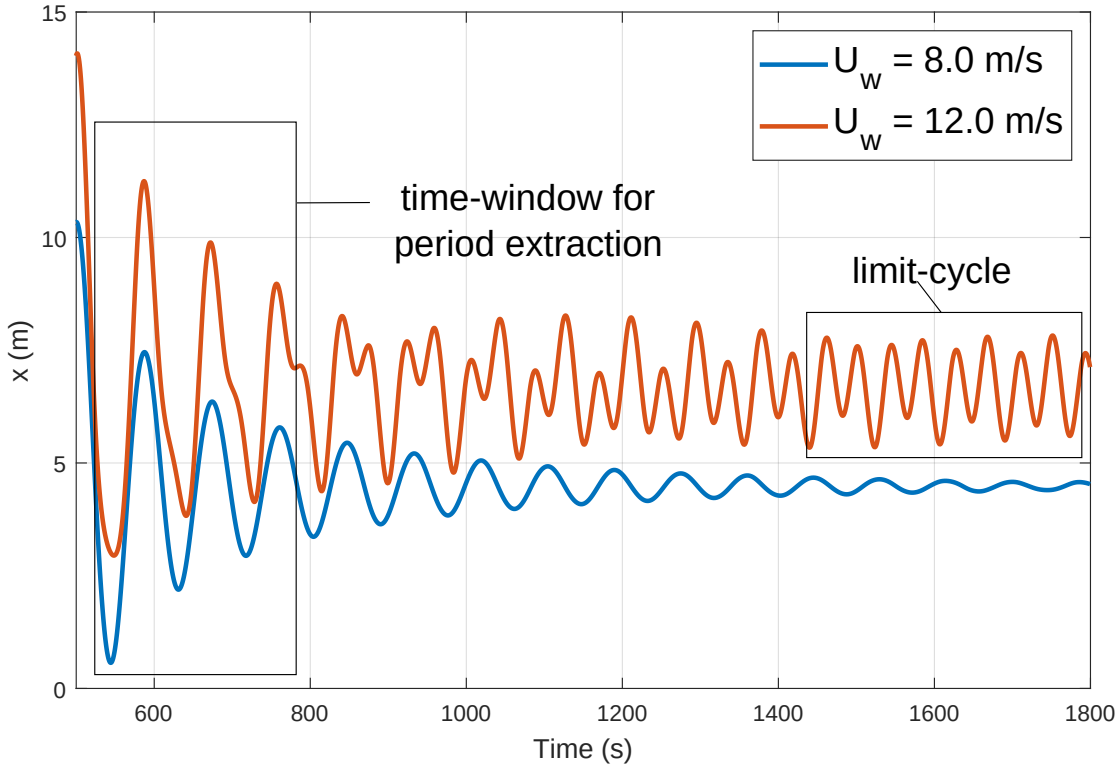

Figure 2: Surge decay time-series for the CSC5MW, under $U_w = 8.0$ m/s and $U_w = 12.0$ m/s.

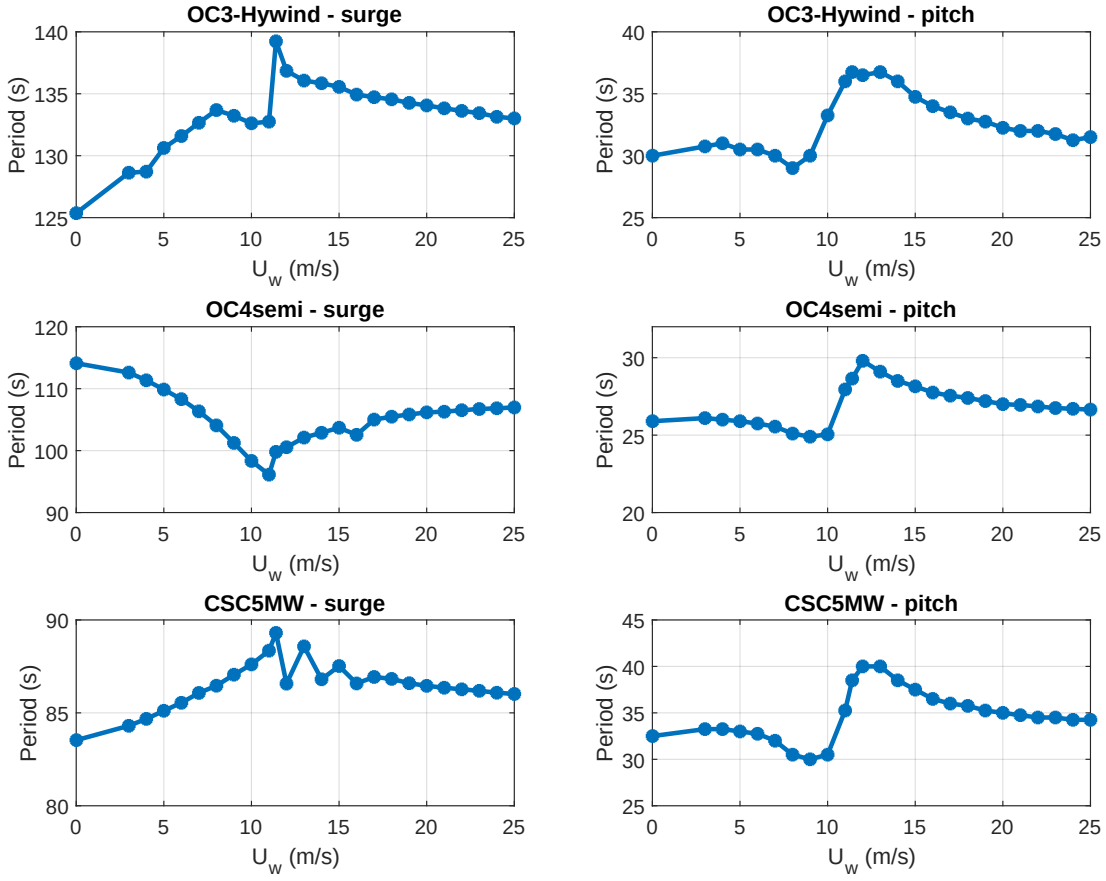

Figure 3: Surge and pitch decay periods for three FWTs considered, under the incident wind velocities of Table 2.

below-rated region, has a minimum near rated wind velocity, and then increases moderately in the above-rated regime.

For pitch decay, as shown in the right-hand column, the pattern is similar for the three concepts: the period is roughly constant until $U_w = 5.0$ m/s, and then decreases until near-rated wind velocity. It is then suddenly increased, reaching its maximum for $U_w \approx 12.0$ m/s – and decreasing from then on. The variations in pitch period may vary in range according to the FWT considered. The OC4semi pitch periods lie inside a range of about 5.0 s; this interval varies more than 10.0 s for the OC3Hywind and CSC5MW.

3. Floating wind turbine dynamics

The simulations presented in the previous section are based on a complete model, including elastic effects and multibody dynamics. Now, a simplified approach is introduced, in which the rigid-body motions of a floating, catenary-moored body are the object of the analysis. The corresponding natural periods are distant from structural flexible modes, while the amplitudes may be 2-3 orders of magnitude higher than those associated with e.g. bending of the tower. Consequently, the following

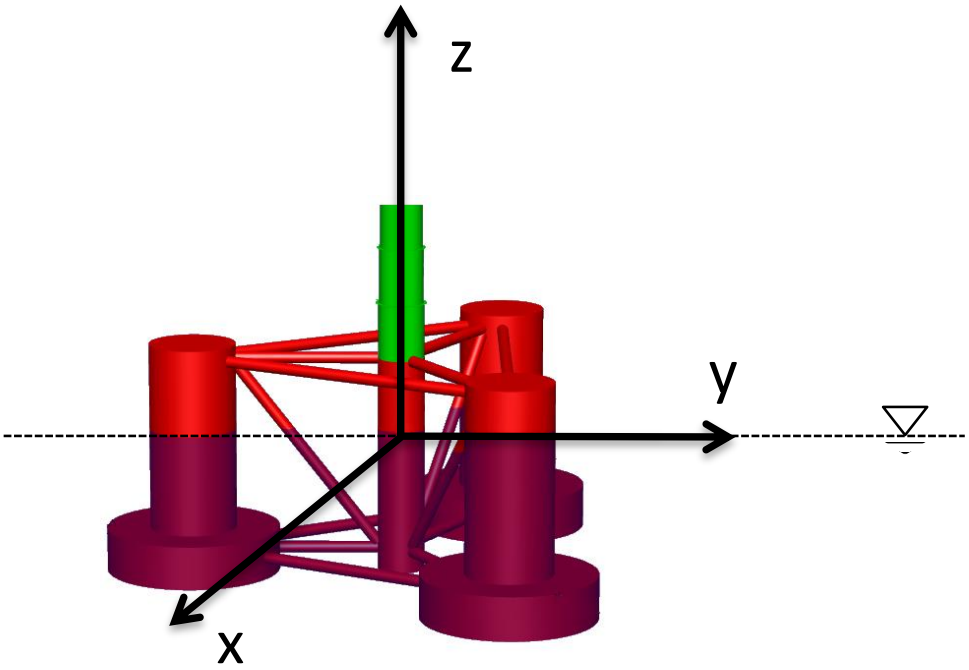

Figure 4: Coordinate system adopted, placed over the OC4semi platform for reference.

single-rigid-body system can be used for representing the dynamic effects of interest [34]:

$$[\mathbf{M}_{RB} + \mathbf{A}_{rad}(\infty)]\,\ddot{\boldsymbol{\eta}} + \int_0^t \mathbf{K}(t-\tau)\dot{\boldsymbol{\eta}}(\tau)d\tau + \mathbf{D}_v(\dot{\boldsymbol{\eta}})\dot{\boldsymbol{\eta}} + [\mathbf{C}_{hs}(\boldsymbol{\eta}) + \mathbf{C}_{mr}(\boldsymbol{\eta})]\,\boldsymbol{\eta} = \mathbf{F}_{ext}\,, \qquad (1)$$

where $\mathbf{M}_{RB}$ is the rigid-body inertia matrix, $\mathbf{A}_{rad}(\infty)$ is the infinite-frequency added mass matrix, $\mathbf{K}$ is a matrix of retardation functions, $\mathbf{D}_v$ is the viscous damping matrix, $\mathbf{C}_{hs}$ and $\mathbf{C}_{mr}$ are the hydrostatic and mooring stiffness matrices, respectively, $\mathbf{F}_{ext}$ is a vector of external loads, and $\boldsymbol{\eta}$ is a vector with the body coordinates in an Earth-fixed coordinate system which has its origin on the water free-surface, with the z-axis pointing upwards (Figure 4).

3.1. Simplified 2-DOF model

The present study considers 0°-winds only – i.e., travelling along the positive x direction. Rotor gyroscopic effects are disregarded, and heave motions are assumed to be entirely decoupled from the other degrees of freedom. Therefore, only surge and pitch dynamics are of interest. Besides, a few assumptions can be proposed to simplify Equation (1) in the analysis of surge and pitch decay:

1. *The platform motions have very low-frequency ($\omega \approx 0$), such that* $\mathbf{K}$ *can be disregarded and the radiation effects can be approximated by replacing* $\mathbf{A}_{rad}(\infty)$ *for* $\mathbf{A}_{rad}(0)$. The reason behind this assumption is the absence of waves and the long natural periods of the floating system's rigid-body motions, corresponding to negligible radiation damping.
2. *The viscous damping can be represented by linear damping only.* This is a reasonable statement considering the low velocities involved.

3. *The hydrostatic and mooring stiffness matrices are independent of the body position.* For the hydrostatic restoring stiffness, this assumption may be justified based on the small changes in volume due to the floater motion, and also on the fairly wall-sided platforms considered in the analysis. With regards to mooring, the matrix has to be linearized around points of interest, since nonlinear effects become important far from the equilibrium position (see Figure 5).
4. *The only external load is the rotor thrust.* This follows from the fact that radiation loads, viscous hydrodynamic forces and mooring/hydrostatic stiffness are already considered in the l.h.s. of the equation, and no waves are present. Besides, wind drag loads on the tower are disregarded.

Equation (1) then reduces to

$$\mathbf{M}\ddot{\boldsymbol{\eta}} + \mathbf{B}_v^l\dot{\boldsymbol{\eta}} + \mathbf{C}\boldsymbol{\eta} = \mathbf{F}_{wind}\,. \tag{2}$$

For a 2-DOF (surge-pitch) system, the matrices in (2) become:

$$\mathbf{M} = \mathbf{M}_{RB} + \mathbf{A}_{rad}(0),\ \mathbf{M}_{RB} = \begin{bmatrix} m & mz_g \\ mz_g & I_{yy} \end{bmatrix},\ \mathbf{A}_{rad}(0) = \begin{bmatrix} a_{11} & a_{15} \\ a_{51} & a_{55} \end{bmatrix},$$

$$\mathbf{B}_v^l = \begin{bmatrix} b_{11} & 0 \\ 0 & b_{55} \end{bmatrix},$$

$$\mathbf{C} = \mathbf{C}_{hs} + \mathbf{C}_{mr},\ \mathbf{C}_{hs} = \begin{bmatrix} 0 & 0 \\ 0 & C_{55}^{hs} \end{bmatrix},\ \mathbf{C}_{mr} = \begin{bmatrix} C_{11}^{mr} & C_{15}^{mr} \\ C_{51}^{mr} & C_{55}^{mr} \end{bmatrix},$$

$$\boldsymbol{\eta} = \begin{bmatrix} x \\ \theta \end{bmatrix},$$

$$\mathbf{F}_{wind} = \begin{bmatrix} F_{aer}\cos\theta \\ F_{aer}z_{hub}\cos^2\theta \end{bmatrix},$$

where m is the total mass of the platform, tower, hub and nacelle; z_g is the system's vertical coordinate of the center of gravity; I_{yy} is the total moment of inertia in pitch; a_{ij} are the zero-frequency added mass coefficients; b_{ii} are the linearized viscous damping coefficients in surge and pitch; C_{55}^{hs} is the linear hydrostatic restoring coefficient in pitch, already accounting for gravitational effects; C_{ij}^{mr} are the linear mooring restoring coefficients; x is the displacement in surge; θ is the pitch angle; F_{aer} is the turbine thrust; and z_{hub} is the hub height.

3.2. Control system

Wind turbines are normally equipped with a control system, in order to optimize power production and interrupt the operation under unfavourable conditions. The NREL 5 MW wind turbine controller

Table 3: Blade-pitch controller gains for zero pitch angle.

$K_p(\beta = 0)$	$K_i(\beta = 0)$
0.6087 s^{-1}	0.0870

actuates on the generator torque (Q_{gen}) and collective blade pitch angle (β), depending on the operational regime.

The generator torque is based on the filtered shaft velocity, ω. In the below-rated regime (3.0 m/s $\leq U_w <$ 11.4 m/s), the torque is proportional to the squared shaft velocity, such as to optimize power production; in the above-rated region (11.4 m/s $\leq U_w \leq$ 25.0 m/s), it is inversely proportional to the shaft velocity, such as to keep the power constant.

In the above-rated regime, the rotor speed is regulated through changes in the blade-pitch angle (which lead to changes in the aerodynamic torque load). The change in blade pitch angle is determined by a gain-scheduled proportional-integral (PI) controller:

$$\Delta\beta = K_p(\beta)\Delta\omega + K_i(\beta)\int_0^t \Delta\omega dt\,, \tag{3}$$

where the proportional (K_p) and integral (K_i) gains are calculated as a function of the blades' current pitch angle, β; see Table 3 for the gains adopted for $\beta = 0$. The input to the controller ($\Delta\omega$) is the difference between the rotor speed and the reference rotor speed. A more detailed description of the control strategy, including the gain scheduling procedure, is provided by Jonkman [22].

3.3. External loads

When a FWT oscillates under the action of wind, it is subjected to three main sources of loads: the aerodynamic thrust, induced on the rotor[3]; the hydrodynamic loads, acting on the submerged portion of the platform; and the mooring loads, applied on the fairleads, which normally are also underwater.

The aerodynamic thrust is a function of the relative flow velocity in the rotor, which is a combination of the incident wind velocity, the nacelle velocity and the inflow velocity. When the turbine oscillates, the nacelle velocity is also oscillatory and so is the thrust. A phase shift, however, is observed between thrust and nacelle velocity. This effect may be worked out and treated as a modification in the nacelle's inertia and damping, therefore influencing the FWT decay periods.

In the absence of waves, hydrodynamic loads may be divided into two groups: the radiation loads, related to the waves produced by the body's motion; and the viscous loads, which are a function of the body's velocity. For typical surge/pitch decay periods ($\omega \approx 0$), radiation loads reduce to acceleration-proportional terms, commonly known as added mass. The added mass influences the natural periods, but there is no reason to relate it to the period *changes* for different wind velocities[4].

[3]The drag on tower and hull should also be classified as an aerodynamic effect, but is of secondary importance and therefore disregarded.

[4]Actually, geometric changes due to variations in the mean pitch offset can affect the radiation loads. This effect is however disregarded in the benchmark simulations presented in Section 2, and therefore are also neglected here.

Viscous damping also affects natural periods, but cannot be used to explain the period variations, either.

Catenary mooring systems normally provide fairly linear stiffness when the platform is close to the neutral position. For surge, however, the stiffness gets nonlinear as the platform is displaced along the x-axis. Therefore, when subjected to a mean wind loading, the platform may oscillate around a mean position which lies in the nonlinear range, leading to a natural period different from when the system oscillates around the neutral position.

It is then expected that the nonlinearities induced by aerodynamic thrust and catenary mooring system should play prevailing roles behind the period variation phenomenon, as discussed below.

4. Prediction of the decay period changes for varying U_w

Simplified representations for the nonlinear effects discussed in the previous section are now developed, providing means to estimate the decay periods based on Equation (2).

4.1. Mooring system nonlinearities

Catenary mooring systems are meant to position a floating body using the mooring lines' own weight-in-water. When the platform is displaced away from the anchor, a portion of the line resting on the seabed is lifted, increasing the weight to be supported by the floater. In addition, due to the change in angle, the horizontal component of the tension increases, also contributing nonlinearly to the horizontal restoring force [14]. The nonlinearity is evident in Figure 5, where the mooring stiffness curves for the three platforms are shown. When subjected to a mean wind force, the platform will oscillate around the corresponding offset, with different stiffnesses – and therefore periods – for varying wind velocities.

Loads induced by catenary mooring systems may be estimated analytically [35]. Here, expressions for the mooring stiffness are instead determined through polynomial fitting of the data in Figure 5. Since the wind displaces the FWT towards the positive x direction, the fitting is made for $x > 0$ only. 3$^{\text{rd}}$-order polynomials are found to fit the data with excellent agreement, such that the following nonlinear stiffness model is applied:

$$F_r(x) = -k_1 x - k_2 x^2 - k_3 x^3 = -k(x)x\,, \tag{4}$$

where k_1, k_2 and k_3 are obtained from the data fitting procedure, and the x-dependent stiffness coefficient is given by:

$$k(x) = k_1 + k_2 x + k_3 x^2\,. \tag{5}$$

Time-domain simulations can be performed by replacing the C_{11}^{mr} element of the stiffness matrix with $k(x)$, calculated according to the procedure above, in Equation (2). Alternatively, the nonlinear model of Equation (4) can be linearized around a given offset x_0. Keeping up to first-order terms in a Taylor expansion, it becomes:

$$F_r(x) \approx (k_2 x_0^2 + 2k_3 x_0^3) - (k_1 + 2k_2 x_0 + 3k_3 x_0^2)x\,, \tag{6}$$

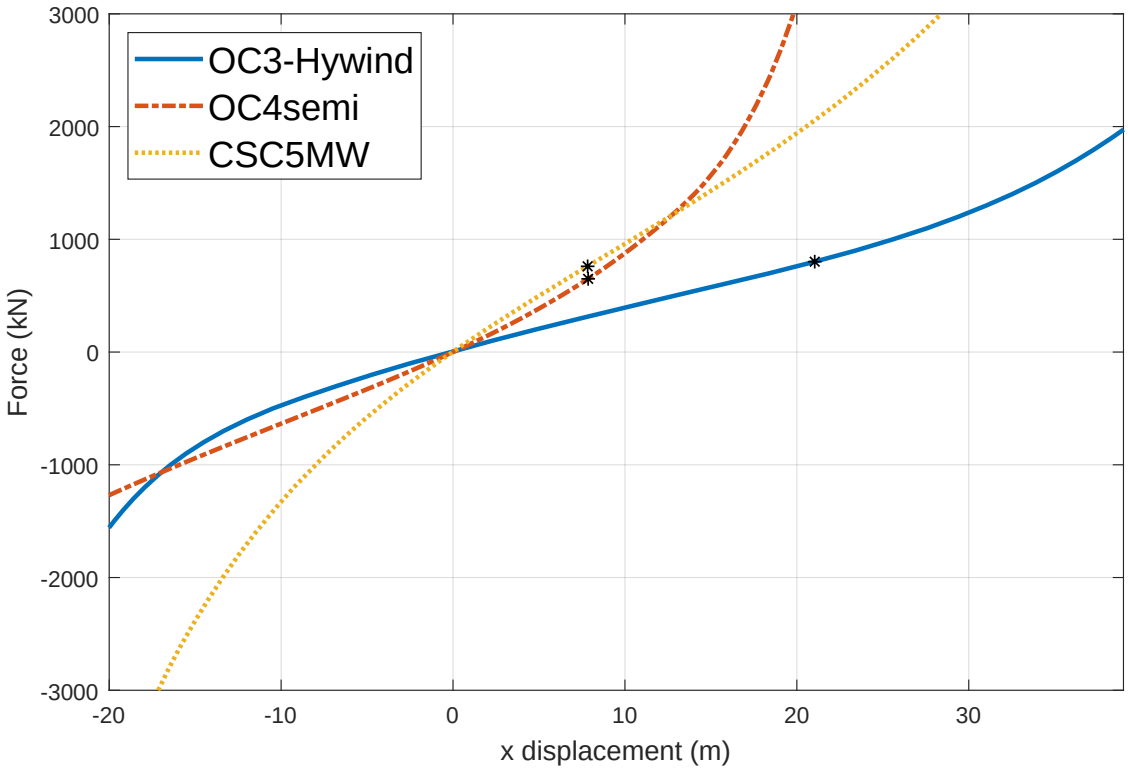

Figure 5: Force-displacement curves obtained from pullout simulations in surge. The asterisks indicate platform displacement for $U_w = 11.4$ m/s. The different offsets in platform pitch explain the slightly different horizontal components of the thrust indicated in the y-axis.

Table 4: Coefficients for the linearized mooring stiffness in surge, as given by Equation (7).

	k_1 (Nm^{-2})	k_2 (Nm^{-3})	k_3 (Nm^{-4})
OC3Hywind	5.37×10^4	-1.44×10^3	3.52×10^1
OC4semi	7.13×10^4	7.52×10^2	8.98×10^1
CSC5MW	1.05×10^5	-1.39×10^3	5.00×10^1

such that the linearized stiffness coefficient k_{11}^{lin} is given by

$$k_{11}^{lin}(x_0) = k_1 + 2k_2x_0 + 3k_3x_0^2\,. \tag{7}$$

Typical platform rotations in pitch do not produce important geometric changes in the mooring lines, resulting in a fairly linear behaviour for the mooring stiffness in this DOF. Therefore, the main source of nonlinear mooring restoring for pitch comes from the surge-pitch coupling, which depends on the vertical distance from the fairleads to the platform's center of gravity.

Still, restoring in pitch for catenary-moored FWTs is dominated by hydrostatic effects – which, for typical pitch angles, have linear behavior. Therefore, mooring stiffness should not be behind the observed changes in the pitch decay period for varying incident wind velocities. The pitch period changes must then be related to the r.h.s. of Equation (2).

4.2. Prediction of the surge decay periods with a linearized stiffness matrix

A simple way to estimate the surge decay periods is to linearize the stiffness around the offset associated to a given U_w, using the x_0 values obtained from the SIMA simulations in Equation (7). The coefficients k_1, k_2 and k_3 for each curve in Figure (5) are presented in Table 4. The cross terms of the mooring stiffness matrix are obtained from the linear stiffness in surge, multiplied by the fairleads vertical position relative to the SWL, z_{fl}, and the term for pitch is kept unchanged. The matrix for a given offset, $\mathbf{C}_{mr}(x_0)$, is then given by:

$$\mathbf{C}_{mr}(x_0) = \begin{bmatrix} k_{11}^{lin}(x_0) & k_{11}^{lin}(x_0)z_{fl} \\ k_{11}^{lin}(x_0)z_{fl} & C_{55}^{mr} \end{bmatrix}\,. \tag{8}$$

The period for each U_w can then be calculated from the eigenvalues of Equation (2), with the stiffness matrix defined as above.

4.3. Aerodynamic apparent inertia/stiffness and damping effects

Let a FWT be subjected to steady, non-turbulent wind. The airflow velocity $w(t)$ is the relative axial flow velocity "felt" by the rotor, and is given by:

$$w(t) = w_0 - w_i(t) - \dot{x}_{nac}\,, \tag{9}$$

where w_0 is the incident wind velocity; $\dot{x}_{nac}$ is the nacelle horizontal velocity; and the inflow velocity, w_i, is a flow induced in the rotor by the vorticity shed by the blades, as stated by the Biot-Savart law.

Platform oscillations affect $w(t)$ through variations in $\dot{x}_{nac}$[5], provoking fluctuations in the rotor torque and thrust. A thorough discussion about this effect is provided by Pedersen [21] – Appendix A summarizes the most relevant formulations from that work for the purposes of this paper. Particularly, important insight is obtained from a combination of equations (A.5) and (A.6), leading to the following expression for the thrust[6]:

$$F = \kappa \left[\cos(u)w - \sin(u)\Omega\ell\right]\Omega\,, \tag{10}$$

where u is the blade-pitch control action, Ω is the rotor angular velocity and κ, ℓ are constants. Noting that $u = 0$ in the below-rated regime (no blade-pitch action), Equation (10) reduces to

$$F = \kappa w \Omega\,. \tag{11}$$

Replacing w as given by (9), and writing the rotor velocity as a mean plus a varying term, $\Omega(t) = \Omega_0 + \Omega'(t)$, the following expression is obtained for the thrust in the below-rated regime:

$$F = \kappa\Omega_0(w_0 - w_i) + \kappa(w_0 - w_i)\Omega' - \kappa\Omega_0\dot{x}_{nac}\,, \tag{12}$$

where only linear terms were kept. Assuming small variations in w_i, the first term in the r.h.s. of Equation (12) may be seen as a constant, while the second term depends essentially on the rotor dynamics. The last term oscillates proportionally to $\dot{x}_{nac}$, and since κ and Ω_0 are both positive, the negative sign implies that the thrust, in the below-rated region, will always induce a damping effect into the nacelle dynamics.

When the turbine operates in the above-rated regime, the blade-pitch control system results in non-zero values for u, and Equation (11) may be rewritten according to:

$$F = \kappa\Omega\left[\cos(u)(w_0 - w_i) - \sin(u)\Omega\ell\right] - \kappa\Omega_0\cos(u)\dot{x}_{nac}\,. \tag{13}$$

The second term now depends on $\cos(u)$, which is a function of the generator angular velocity through a PI-controller. Therefore, it is no longer possible to affirm that the oscillating term is proportional to $-\dot{x}_{nac}$. While an analytical development of this relation is not in the scope of this paper, it is of interest to understand how F varies as a function of $\dot{x}_{nac}$ in the above-rated regime, and the consequent effects on the system global dynamics.

For this purpose, a series of simulations were executed in which the NREL 5 MW turbine (including controller) oscillated horizontally, with rotor aerodynamics calculated with AeroDyn [36]. It was decided to adopt the BEM formulation with dynamic stall correction, and the blades were kept rigid. The oscillation amplitude was 10.0 m and the period varied from 20.0 s to 160.0 s, with increments of 1.0 s. The incident wind velocities are the same as those presented in Table 2.

Figure 6 shows the aerodynamic thrust and nacelle velocity for an oscillation period of 30.0 s and incident wind velocities of 9.0 m/s, 11.4 m/s and 18.0 m/s. It is suggested that the thrust F can be

[5]The inflow velocity w_i is also affected, but in a much lower degree.

[6]Note that equation (A.6) actually refers to the *circulatory thrust* only – i.e., the drag portion (A.7) is disregarded in this discussion, due to its relatively lower importance.

written as a sum of a mean term, $F_{mean}(U_w)$, and a varying term, $F_{var}(U_w, \dot{x}_{nac})$:

$$F_{aer} = F_{mean}(U_w) + F_{var}(U_w, \dot{x}_{nac})\,. \tag{14}$$

For $U_w = 9.0$ m/s, the phase difference between F_{var} and $\dot{x}_{nac}$ is close to π rad, which is in agreement

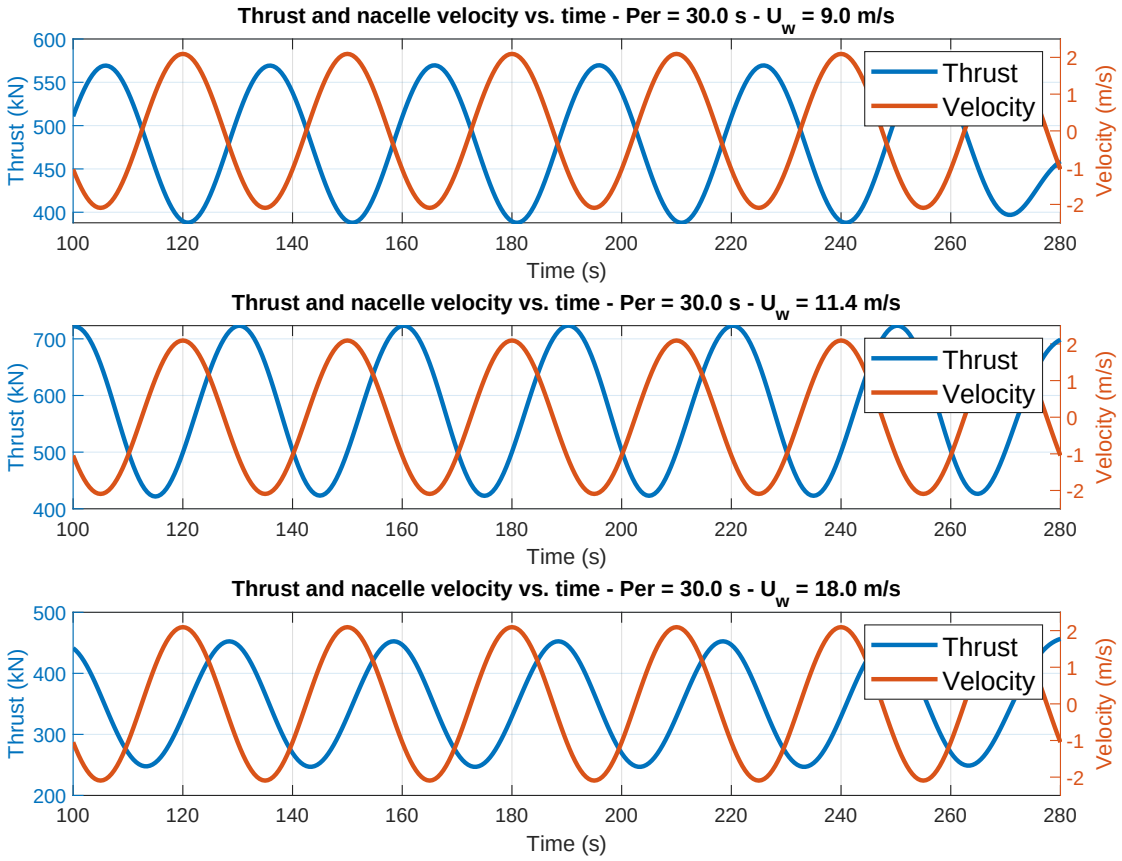

Figure 6: Aerodynamic thrust and nacelle velocity from forced oscillations of the NREL 5 MW reference wind turbine, with amplitude of 10.0 m, oscillation period of 30.0 s and $U_w = 9.0$ m/s, 11.4 m/s and 18.0 m/s.

with the discussion above. Defining a *velocity-to-thrust amplitude factor* f_0, $F_{var}(U_w, \dot{x}_{nac})$ may be rewritten as follows:

$$F_{var}(U_w, \dot{x}_{nac}) \approx -f_0 \dot{x}_{nac}\,. \tag{15}$$

The 1-DOF motion of the nacelle, with mass m, stiffness k and damping c, and forced by F, is driven by:

$$m\ddot{x} + c\dot{x} + kx = F_{mean} - f_0\dot{x} \implies m\ddot{x} + (c + f_0)\,\dot{x} + kx = F_{mean}\,, \tag{16}$$

where the *nac* indicator on x was suppressed for conciseness.

The discussed damping effect of the thrust is now more visible. This is a well-known effect for FWTs, explained e.g. in [7, 25]. The second and third plots of Figure 6, however, show that the controller action results in the thrust oscillating with a phase ϕ relative to the nacelle velocity. This effect, also reported in [37], is not fully understood yet, but dynamic wake effects, actuator dynamics and delays induced by signal filtering may possibly contribute to it.

Assuming that the nacelle motion may be described as $x(t) = x_0 \sin(\omega t)$, the velocity is given by $\dot{x}(t) = x_0 \omega \cos(\omega t)$, and F_{var} becomes

$$\begin{aligned} F_{var} &= f_0 x_0 \omega \cos(\omega t + \phi) \\ &= f_0 \left[x_0 \omega \cos(\omega t) \cos(\phi) - x_0 \omega \sin(\omega t) \sin(\phi) \right] \\ &= f_0 \left[\dot{x} \cos(\phi) - \omega x \sin(\phi) \right] . \end{aligned} \tag{17}$$

Noting that

$$\omega x = \frac{\omega^2}{\omega} x = -\frac{\ddot{x}}{\omega} ,$$

the last term of Equation (17) can then alternatively be written as:

$$F_{var} = f_0 \left[\dot{x} \cos(\phi) + \frac{\ddot{x}}{\omega} \sin(\phi) \right] . \tag{18}$$

In the above-rated regime the thrust is thus no longer proportional to the nacelle velocity only, but rather to a combination of nacelle velocity and position/acceleration. In the latter case, the effect may be interpreted as an "apparent inertia":

$$\left[m - \frac{f_0}{\omega} \sin(\phi) \right] \ddot{x} + \left[c - f_0 \cos(\phi) \right] \dot{x} + kx = F_{mean} . \tag{19}$$

Variations in the system's natural period can now be related to f_0 and ϕ. When the phase is such that $|\sin(\phi)|$ increases, the thrust effect on the system's damping is reduced and the apparent changes in inertia become more important. A quantification of this influence demands a better understanding on how f_0 and ϕ vary with the incident wind velocity, the nacelle's period of oscillation and the motion amplitude.

4.4. Quantification of the apparent inertia and damping effects induced by the thrust

The above-mentioned simulations with AeroDyn provided a total of 3384 pairs of rotor thrust and nacelle velocity time-series. For each pair, a *fast Fourier transform* (FFT) was performed for both time-series, yielding their discrete frequency domain representations. The phase ϕ between the time-series could then be determined as the angle of the ratio between the thrust and nacelle velocity representations in the frequency domain, at the frequency of oscillation. The velocity-to-thrust amplitude factor, f_0, is obtained directly from the time-series, by considering the ratio of their maximum amplitudes.

Figure 7 shows the values of ϕ calculated as explained above. One can clearly distinguish the below-rated region by the nearly uniform phase values – close to π rad, as discussed previously. Close to $U_w = 11.4$ m/s, the phase values change smoothly for shorter oscillation periods, lying between $\pi/6$ rad and $2\pi/3$ rad as the wind velocity increases. When the period is longer, the change is more abrupt and the phase tends to be smaller, lying between 0 rad and $\pi/6$ rad. This indicates that, when the system dynamics are slower, the thrust tends to follow the velocity more closely.

Another important feature of the plot is that it helps to visualize the operating conditions when, according to Equation (19), the thrust results in a negative damping effect – i.e., when the phase lies between 0 rad and $\pi/2$ rad. This is observed for most of the above-rated region, but for shorter

periods and wind velocities closer to rated, the phase may be slightly higher than $\pi/2$ rad. This may be useful e.g. during the design of a controller.

The f_0 factor values are presented in a similar scheme, in Figure 8. In general, the factor changes more intensely near rated wind velocity, where it is highly amplified in comparison to other operational regions. The thrust amplitude changes much faster from below rated to rated when the periods are longer, while this transition is smoother for shorter periods.

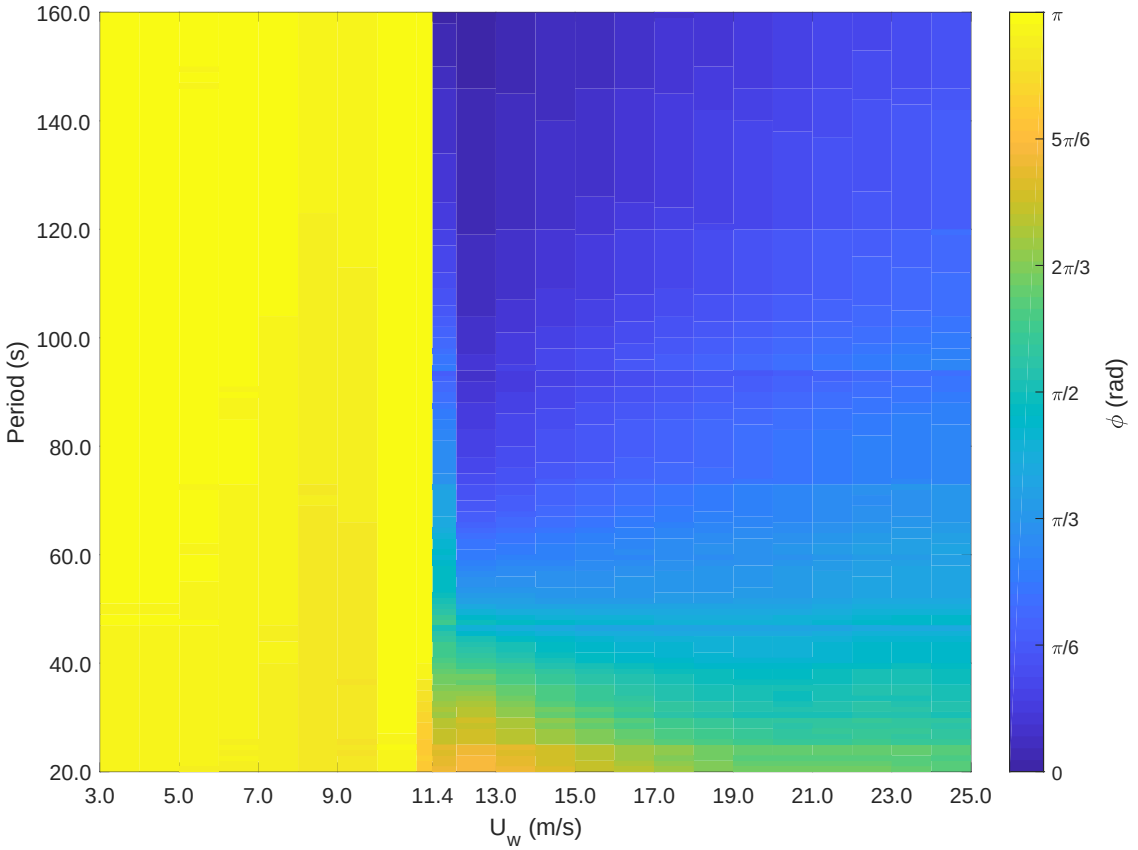

Figure 7: Phases between rotor thrust and nacelle velocity (ϕ) as a function of incident wind velocity and oscillation period.

Once ϕ and f_0 are known, the apparent inertia and damping from thrust can be quantified. From Equation (19), the aerodynamic apparent inertia and damping coefficients, a_{aer} and b_{aer}, are defined according to:

$$a_{aer} = -\frac{f_0}{\omega}\sin(\phi)\,, \quad b_{aer} = -f_0\cos(\phi) \tag{20}$$

The matrices of aerodynamic apparent inertia and damping can then be written as:

$$\mathbf{A}_{aer} = \begin{bmatrix} a_{aer} & a_{aer}h_{nac} \\ a_{aer}h_{nac} & a_{aer}h_{nac}^2 \end{bmatrix}, \tag{21}$$

$$\mathbf{B}_{aer} = \begin{bmatrix} b_{aer} & b_{aer}h_{nac} \\ b_{aer}h_{nac} & b_{aer}h_{nac}^2 \end{bmatrix}, \tag{22}$$

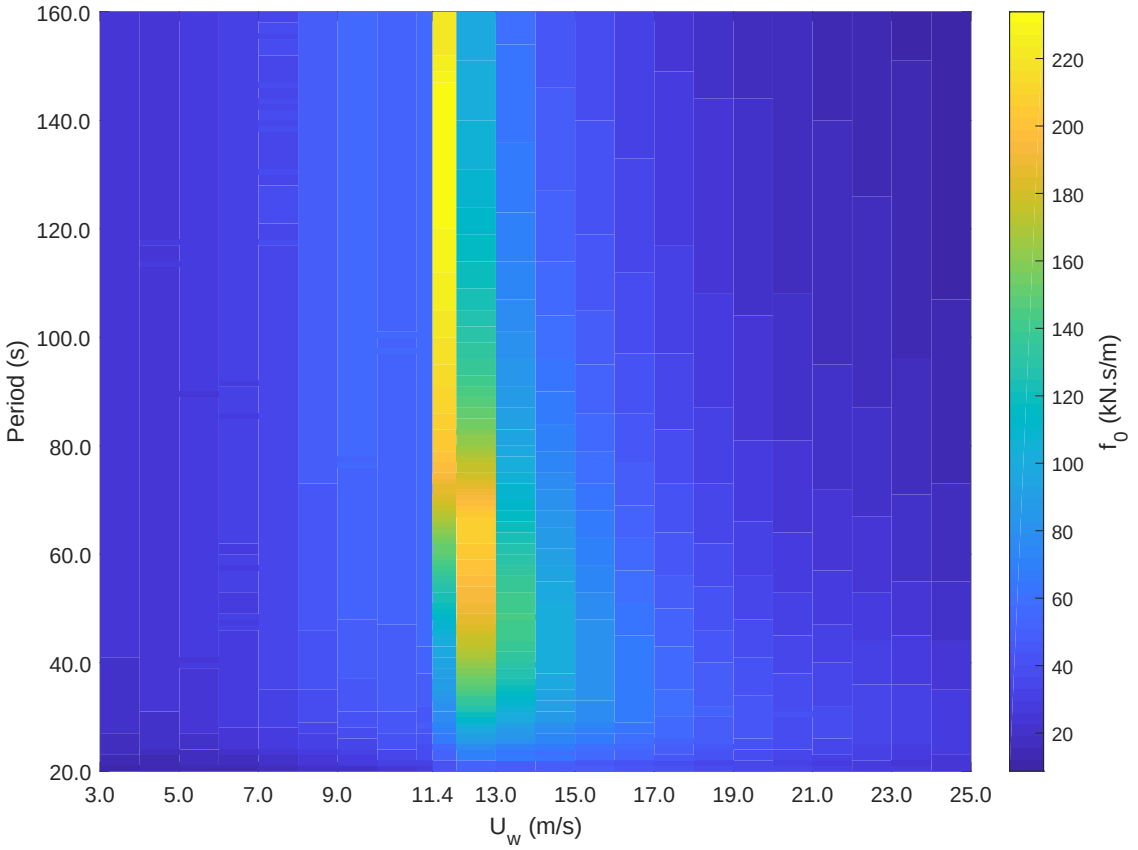

Figure 8: Velocity-to-thrust amplitude factor (f_0) as a function of incident wind velocity and oscillation period.

where h_{nac} is the height of the nacelle with respect to SWL.

One should note that Figures 7 and 8 are based on *imposed* nacelle oscillations – i.e., the motions are not affected by the thrust. This is in contrast with the decay simulations, in which the motions are not only influenced by the thrust but also indirectly modify it through the changes in flow velocity and varying rotor speed. Indeed, the second term on the r.h.s. of Equation (12) depends on Ω', whose dynamics are given by:

$$\dot{\Omega}' = \frac{Q_{aer} - Q_{gen}}{I_{rot}}\,, \tag{23}$$

where Q_{aer} and Q_{gen} are the aerodynamic and generator torque, respectively, and I_{rot} is the rotor moment of inertia around the shaft. From Equation (A.6) and the discussions in section 3.2, the dependence of Ω' on both $\dot{x}_{nac}$ and Ω become evident, but this is not captured by the proposed model. Inaccuracies on the period predictions are therefore expected especially in the below-rated regime. Above-rated, the torque regulation through blade-pitch control reduces the importance of the rotor dynamics, leading to more accurate period predictions.

4.5. Prediction of the pitch decay periods based on the apparent inertia and damping effects

The aerodynamic effects on inertia and damping can be accounted for in the FWT dynamics by adding $\mathbf{A}_{aer}$ and $\mathbf{B}_{aer}$ to the inertia and damping matrices:

$$\mathbf{M}' = \mathbf{M}_{RB} + \mathbf{A}_{rad}(0) + \mathbf{A}_{aer}\,, \tag{24}$$

$$\mathbf{B}' = \mathbf{B}_{v}^{l} + \mathbf{B}_{aer}\,, \tag{25}$$

such that Equation (2) can now be rewritten as follows:

$$\mathbf{M}'\ddot{\boldsymbol{\eta}} + \mathbf{B}'\dot{\boldsymbol{\eta}} + \mathbf{C}\boldsymbol{\eta} = \bar{\mathbf{F}}_{wind}\,, \tag{26}$$

where $\bar{\mathbf{F}}_{wind}$ is formed by the mean thrust component, F_{mean}:

$$\bar{\mathbf{F}}_{wind} = \begin{bmatrix} F_{mean} \\ F_{mean} z_{hub} \end{bmatrix}. \tag{27}$$

It is assumed in Equation (27) that the pitch angle is small enough for the dependence in θ to be neglected. As it is noted, the varying component of the thrust is now "absorbed" by the inertia and damping matrices, making it straightforward to relate its effects to changes in the decay periods for different incident wind velocities.

The pitch decay period for a given U_w can be calculated once the coefficients a_{aer} and b_{aer} are known. These coefficients, however, depend themselves on the period, such that an iterative procedure is adopted. Departing from an initial guess for the period, the phase ϕ and the amplitude factor f_0 are obtained by interpolation in the matrices presented in Figures 7 and 8. A new value for the period is then obtained based on the corresponding a_{aer} and b_{aer}, and is compared to the previous guess. The process is repeated until the difference becomes lower than a given tolerance.

The relevance of the apparent inertia can now be assessed. Table 5 shows the ratio between the apparent inertia and the rigid-body plus zero-frequency added inertia, in surge (top) and pitch (bottom), for three values of U_w. For surge, the effect of apparent inertia is irrelevant for the below- and above-rated regimes, while near rated the value may have some importance[7]. For pitch, the apparent inertia is again negligible at the below-rated region. For above-rated, however, the nacelle apparent inertia assumes values that, when multiplied by the squared nacelle height, may result in an apparent moment of inertia effect with order of magnitude comparable to the FWT's rigid-body and added inertia, depending on the platform.

The apparent damping effect is relevant for both surge and pitch. As indicated in Table 6, for below-rated wind speeds it may significantly increase the viscous damping at both DOFs. For $U_w = 11.4$ m/s, however, the damping assumes a negative value in surge, even exceeding the equivalent linear viscous coefficient for the OC4semi. In the SIMA simulations (where the damping is a combination

[7]Figure 7 shows however that for periods higher than 90.0 s the change in phase at 11.4 m/s is quite sudden, such that one should be careful with the phases (and therefore inertia/damping effects) calculated for this wind speed.

Table 5: Ratio (%) between aerodynamic apparent mass and rigid-body+added mass.

		$U_w = 7.0$ m/s	$U_w = 11.4$ m/s	$U_w = 18.0$ m/s
surge $\frac{a_{aer}}{(m+a_{11})}$	OC3Hywind	0.04	2.60	1.57
	OC4semi	0.01	6.55	0.60
	CSC5MW	0.30	8.99	0.28
pitch $\frac{a_{aer}h_{hub}^2}{(I_{yy}+a_{55})}$	OC3Hywind	0.05	3.19	1.93
	OC4semi	0.22	10.02	8.22
	CSC5MW	0.53	18.81	10.77

Table 6: Ratio (%) between aerodynamic apparent damping and linear viscous damping.

		$U_w = 7.0$ m/s	$U_w = 11.4$ m/s	$U_w = 18.0$ m/s
surge $\frac{b_{aer}}{b_{11}}$	OC3Hywind	21.80	−92.78	−13.95
	OC4semi	45.11	−140.43	−31.28
	CSC5MW	24.98	−62.49	−20.67
pitch $\frac{b_{aer}h_{hub}^2}{b_{55}}$	OC3Hywind	19.89	18.10	−5.37
	OC4semi	60.27	73.18	−11.65
	CSC5MW	83.47	45.12	−25.07

of linear and quadratic terms), this results in an effective zero-damping scenario, leading to the limit-cycle effect discussed in section 2.3. For pitch, however, the damping is still positive at rated, but becomes negative for all platforms as the wind velocity increases.

5. Results

The natural frequencies for each U_w are obtained from the eigenvalues of the undamped and homogeneous version of Equation (2):

$$\mathbf{M}\ddot{\boldsymbol{\eta}} + \mathbf{C}\boldsymbol{\eta} = \mathbf{0}\,, \tag{28}$$

where for surge the mooring stiffness matrix is written as in Equation (8), while for pitch the inertia matrix includes $\mathbf{A}_{aer}$, as given by Equation (24). The undamped natural frequency for a given DOF, $\omega_{0,i}$, is then corrected for accounting for damping, yielding the decay frequency $\omega_{d,i}$:

$$\omega_{d,i} = \omega_{0,i}\sqrt{1-\zeta_i^2}\,, \tag{29}$$

where ζ_i is the relative damping coefficient. While for surge it is based on the b_{11} coefficients from Section 3, for pitch it also accounts for the main diagonal elements of the matrix given in Equation (22).

5.1. Periods in surge

The predicted surge periods are presented in Figures 9–11, which show the estimates for the three FWT concepts considered, under the range of incident wind velocities of Table 2. The bottom plots

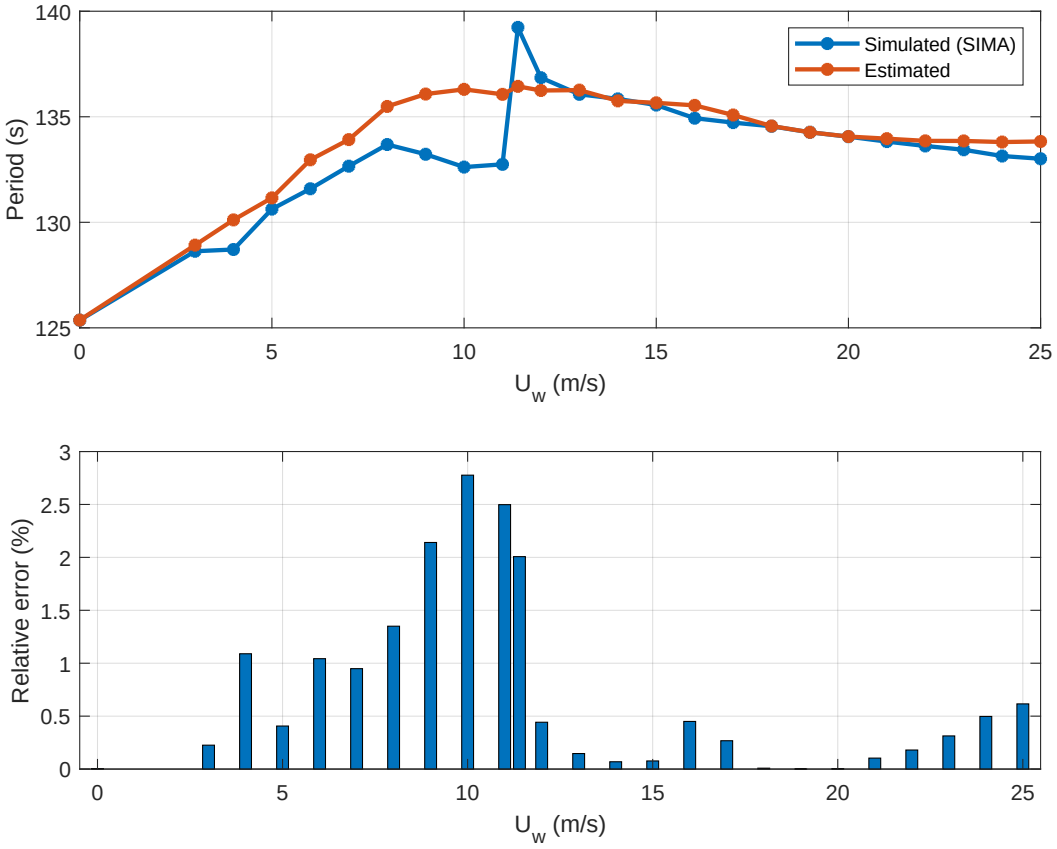

Figure 9: Surge decay periods: simulations with SIMA and estimates based on Equation (2), with mooring stiffness matrix according to Equation (8) – OC3-Hywind.

bring the relative error between estimated and simulated periods.

For the OC3-Hywind (Figure 9), the estimated periods match the simulations with an error in general lower than 0.5% in the above-rated regime. For the below-rated region there is an increase in the relative error as the wind speed approaches the rated condition, notably for U_w = 8.0–11.0 m/s. At this range of wind speeds, the platform offsets in surge are not so different from what is observed for U_w = 12.0–16.0 m/s, where the discrepancy between simulations and estimates is much lower. This suggests that the discrepancies may hardly be attributed to the linearization method adopted.

The agreement between estimated and simulated periods is much better for the OC4semi (Figure 10) and the CSC5MW (Figure 11). Indeed, the relative error for both FWTs is lower than 1% for most U_w values, increasing only near rated wind velocity.

5.2. Periods in pitch

Figures 12–14 show the estimated decay periods in pitch for the three FWT concepts considered, under the range of incident wind velocities of Table 2. For all three concepts, it is seen that the period variation from the SIMA simulations is very satisfactorily followed by the estimates in the rated and above-rated regime. For the OC3Hywind, the relative error for U_w = 11.4 m/s is around 4%, lying below 2% for higher velocities. For the OC4semi and CSC5MW the relative errors are even smaller, with simulated and estimated curves nearly coincident along the above-rated regime. In the

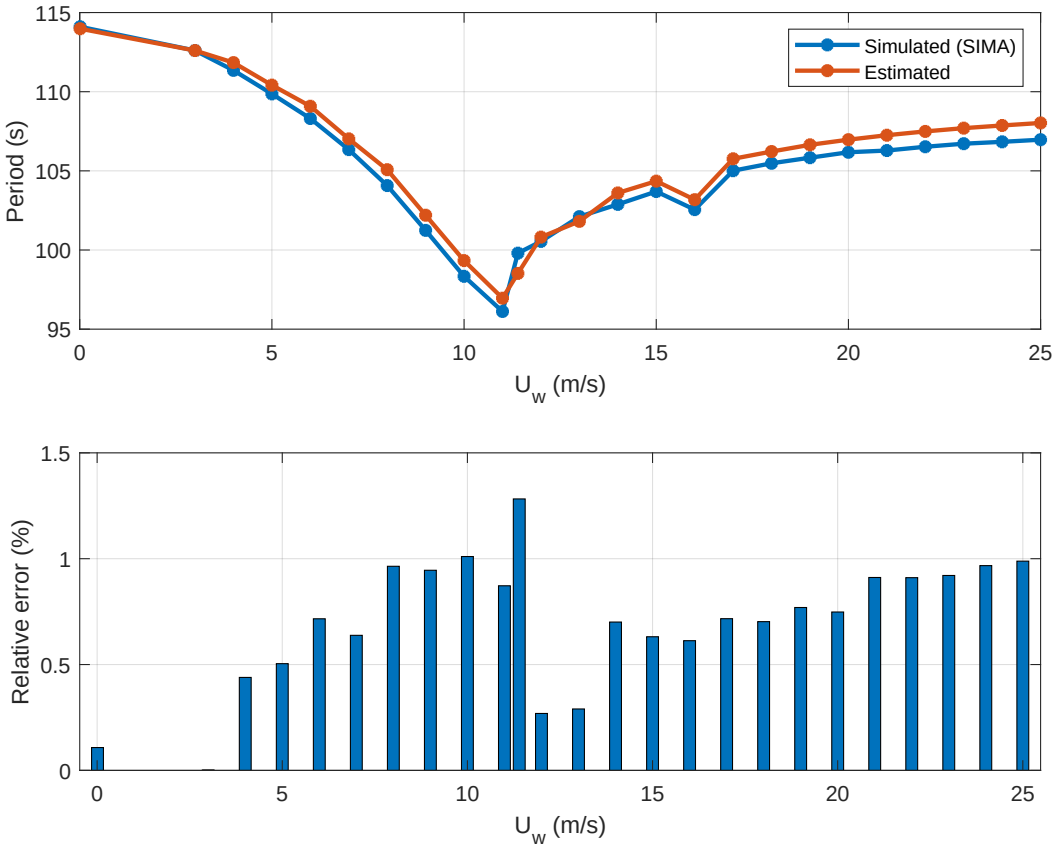

Figure 10: Surge decay periods: simulations with SIMA and estimates based on Equation (2), with mooring stiffness matrix according to Equation (8) – OC4semi.

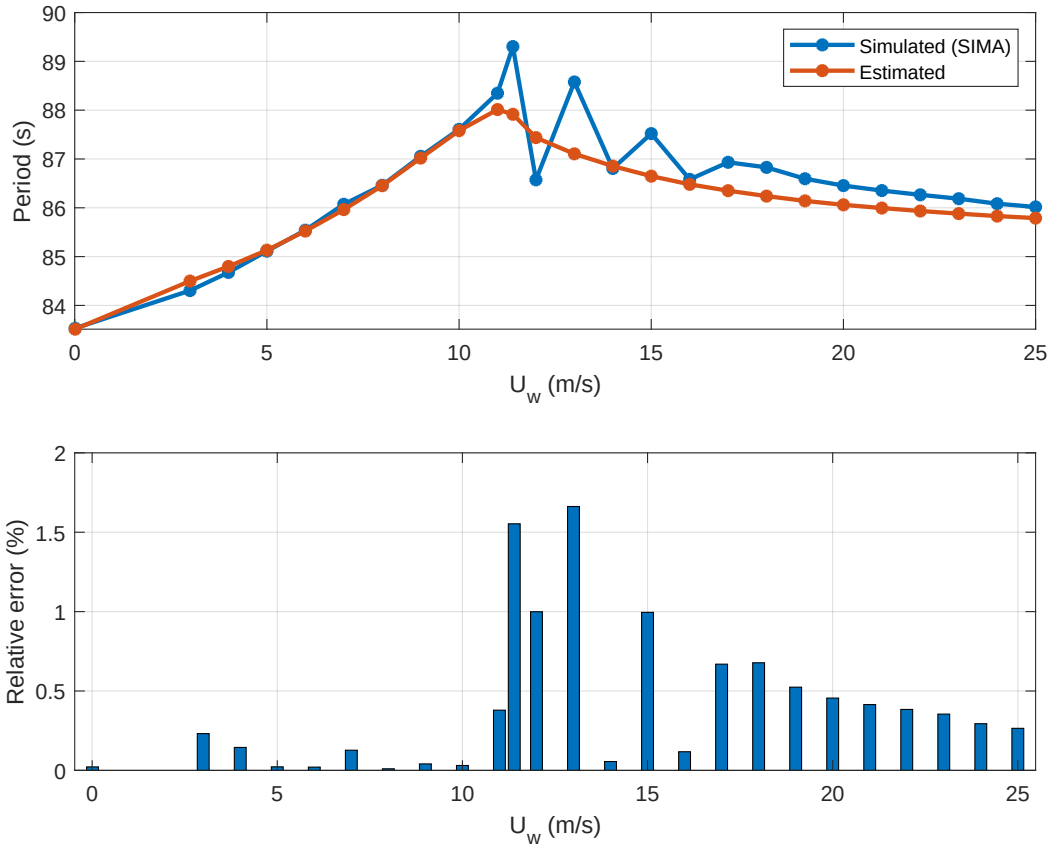

Figure 11: Surge decay periods: simulations with SIMA and estimates based on Equation (2), with mooring stiffness matrix according to Equation (8) – CSC5MW.

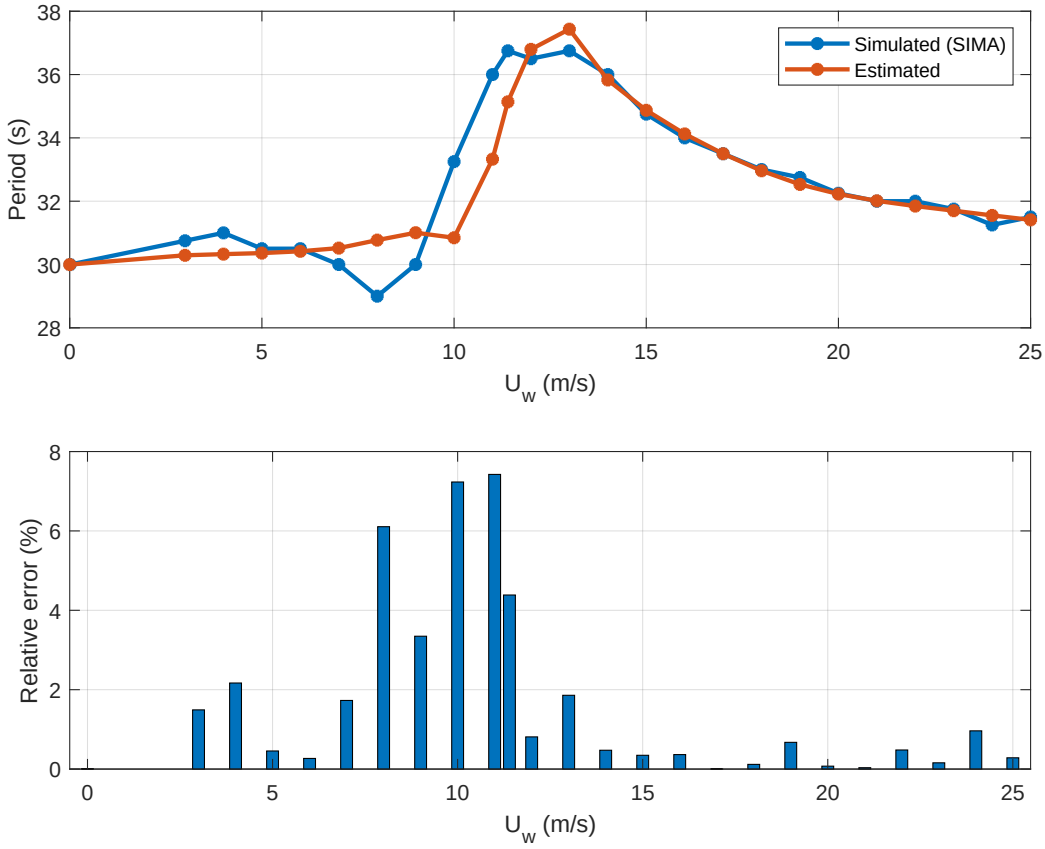

Figure 12: Pitch decay periods: simulations with SIMA and estimates based on Equation (26) – OC3-Hywind.

below-rated region, however, the estimates for all concepts fail to predict a "depression" observed for the simulated periods in the range 6.0 m/s $\geq U_w \geq$ 10.0 m/s. A possible explanation may be the absence, in the simplified model, of the influence of the rotor dynamics – as discussed in section 4.4.

Even though all three FWT concepts are equipped with the same turbine, the magnitude of the period changes is not the same, as already pointed out in Section 2.3. This can be related to the fact that the natural periods (for $U_w = 0$) differ for each design, falling in different regions of Figure 7. Indeed, Figure 7 shows that at the range of periods between 20.0 s and 40.0 s the phases vary significantly in the above-rated regime, implying that modest changes in the FWT inertia properties may heavily influence the period variation phenomenon.

6. Conclusions

As previously reported in [6, 7], surge and pitch decay periods variations were observed for FWTs operating under different incident wind velocities. In this paper, the effect was reproduced in time-domain simulations performed with SIMA, and an investigation for its origins was carried out. It was found that the period variations in surge and pitch have distinct sources. While for the former the effect is mainly linked to the mooring system nonlinearities, for the latter it is induced by the thrust at the turbine, in combination with the nacelle motions.

A simplified model was then applied for predicting the period variations as a function of the

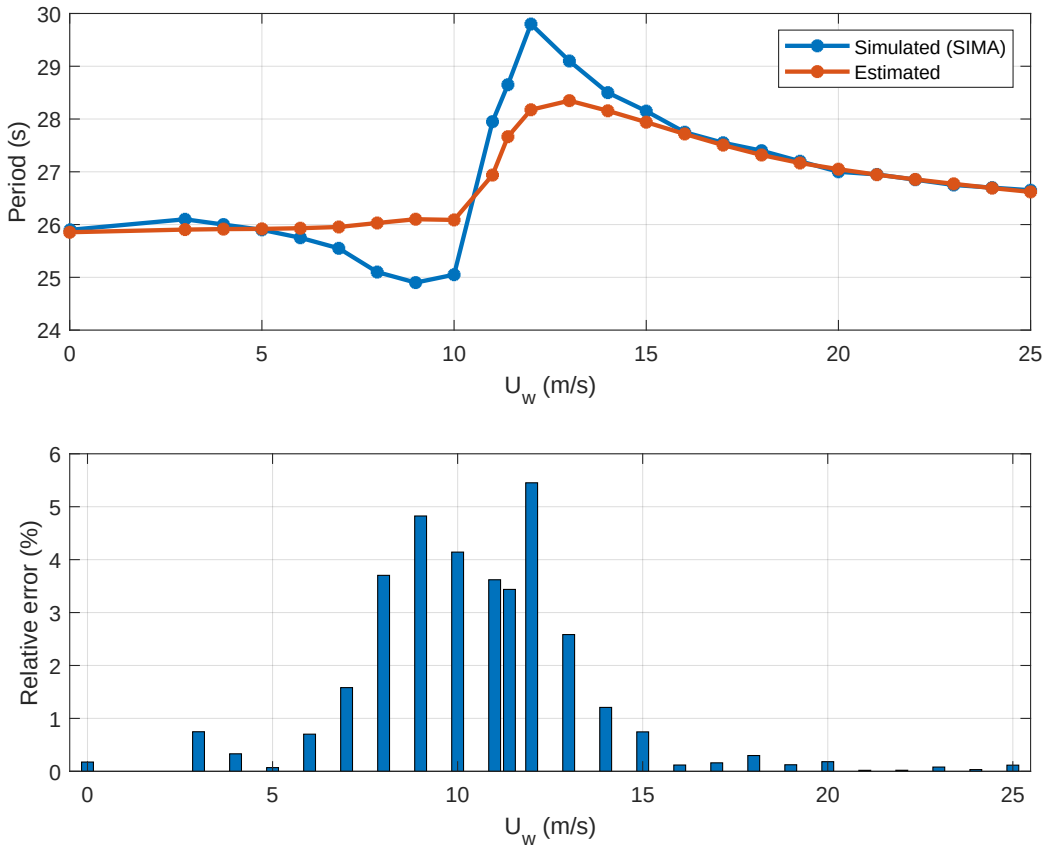

Figure 13: Pitch decay periods: simulations with SIMA and estimates based on Equation (26) – OC4semi.

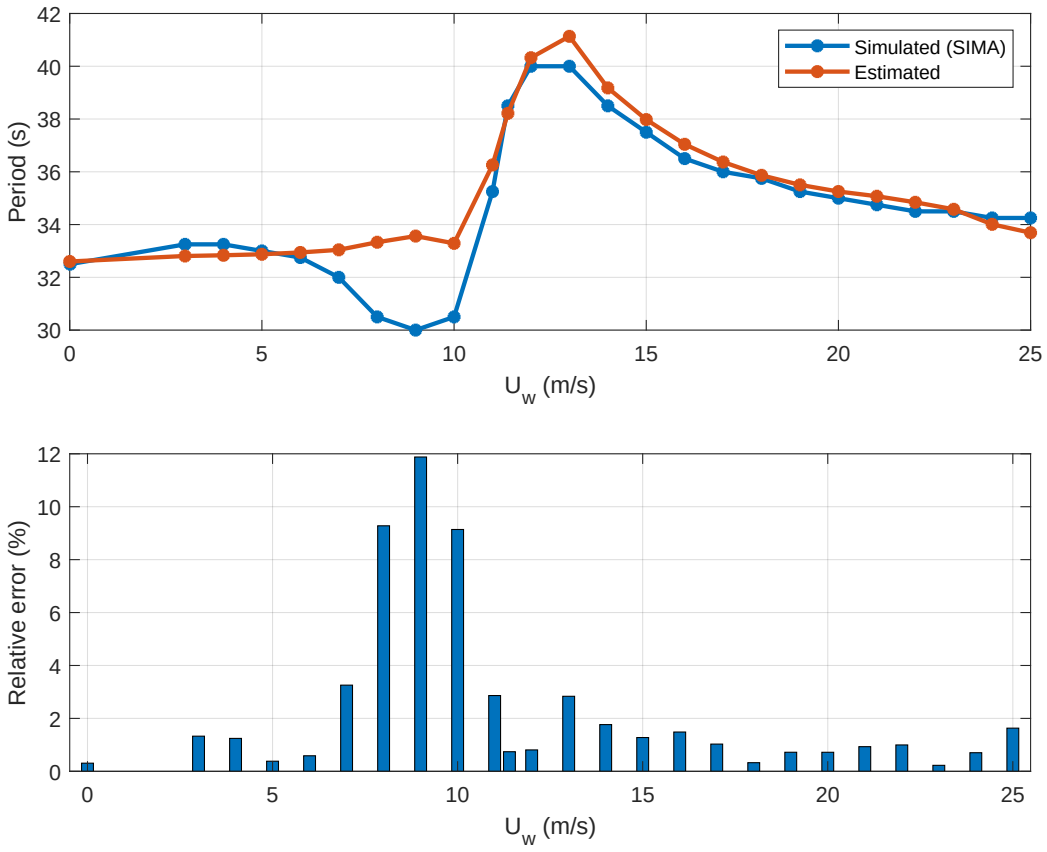

Figure 14: Pitch decay periods: simulations with SIMA and estimates based on Equation (26) – CSC5MW.

incident wind velocity. For surge, the mooring stiffness coefficient was linearized around the offsets associated to each U_w, and then the periods were found from the eigenvalues of the linear 2-DOF equation of motion. The predictions closely agreed with the simulated periods, with relative errors of less than 1% along most of the range of U_w values. Higher (but still limited) discrepancies were observed close to rated regime.

For pitch, the relative phase between nacelle velocity and the thrust induced in the rotor could be related to apparent inertia and damping terms in the equations of motion. This effect was quantified for a combination of wind velocities and oscillation periods, through simulations involving AeroDyn coupled to an 1-DOF system. Inertia and damping coefficients were then included in a linear model, from which the periods could be estimated. The method resulted in precise predictions of the period in comparison with the time-domain simulations, in the above-rated region. In the below-rated region, a "depression" was noticed for the simulated data which could not be replicated with the approximated method. The reasons for this discrepancy are unclear, but a possible explanation could be that the phases and amplitudes from Figures 7 and 8 are based on imposed nacelle oscillations, which did not depend on the thrust – and rotor dynamics – in a coupled manner. A better understanding of this coupling effect and how to include it in the simplified model would represent important contributions to the method.

The period variation in pitch depended on the height of the nacelle relative to SWL. The effect is expected to be more relevant for higher towers, and thus more important for turbines of higher capacity. On the other hand, the phenomenon can be attenuated by proper tuning of the FWT's own pitch natural period, by "placing" the oscillations in a range where the apparent inertia effect is less relevant.

The capability of predicting the period variation with a simplified method may be useful in different stages of the development of new FWT concepts. For example, the possibility of replacing full decay simulations (which took approximately 15 min, with an Intel® Core™i7 6500U 2.50 GHz CPU, for each wind velocity) for eigenvalues calculations (0.8 s for the entire range of wind velocities) can be an advantage when different platform concepts are to be considered in early design phases. Further research may relate the proposed method to disciplines like structural integrity assessment, control system design, mooring systems and model testing. The method could also contribute in the development of new frequency-domain tools.

Acknowledgements

The authors are sincerely grateful to the financial support from NTNU/IMT and the Centre for Autonomous Marine Operations and Systems (AMOS).

References

[1] PrinciplePower, Windfloat (2014).
URL http://www.principlepowerinc.com/en/windfloat(visitedonMarch,2016)

[2] Fukushima FORWARD, Fukushima offshore wind consortium (2016).
URL http://www.fukushima-forward.jp/english/index.html

[3] Equinor, How Hywind works (2018).
URL https://www.equinor.com/en/what-we-do/hywind-where-the-wind-takes-us/hywind-up-close-and-personal.html

[4] LIFES50+, Innovative floating offshore wind energy (2015).
URL http://lifes50plus.eu/

[5] F. Lemmer, F. Amann, S. Raach, D. Schlipf, Definition of the SWE-TripleSpar floating platform for the DTU 10MW reference wind turbine (2016).
URL http://www.ifb.uni-stuttgart.de/windenergie/downloads

[6] E. E. Bachynski, M. Thys, T. Sauder, V. Chabaud, L. O. Saether, Real-time hybrid model testing of a braceless semi-submersible wind turbine. Part II: Experimental results, in: Proceedings of the ASME 35th International Conference on Ocean, Offshore and Arctic Engineering (OMAE2016), Busan, Korea, 2016.

[7] A. J. Goupee, R. W. Kimball, H. J. Dagher, Experimental observations of active blade pitch and generator control influence on floating wind turbine response 104 (2017) 9 – 19. doi:http://dx.doi.org/10.1016/j.renene.2016.11.062.

[8] R. Lupton, Frequency-domain modelling of floating wind turbines, Ph.D. thesis, University of Cambridge, Cambridge, United Kingdom (2014).

[9] A. Pegalajar-Jurado, M. Borg, H. Bredmose, An efficient frequency-domain model for quick load analysis of floating offshore wind turbines, Wind Energy Science Discussions 2018 (2018) 1–30. doi:10.5194/wes-2018-25.
URL https://www.wind-energ-sci-discuss.net/wes-2018-25/

[10] H. Ormberg, K. Larsen, Coupled analysis of floater motion and mooring dynamics for a turret-moored ship, Applied Ocean Research 20 (1) (1998) 55 – 67. doi:https://doi.org/10.1016/S0141-1187(98)00012-1.

[11] H. Ormberg, E. Passano, N. Luxcey, Global analysis of a floating wind turbine using an aero-hydro-elastic model. Part 1: code development and case study, in: Proceedings of the ASME 2011 30th International Conference on Ocean, Offshore and Arctic Engineering (OMAE2011), 2011.

[12] N. Luxcey, H. Ormberg, E. Passano, Global analysis of a floating wind turbine using an aero-hydro-elastic model. Part 2: benchmark study, in: Proceedings of the ASME 2011 30th International Conference on Ocean, Offshore and Arctic Engineering (OMAE2011), 2011.

[13] J. M. Jonkman, Dynamics modeling and loads analysis of an offshore floating wind turbine, Ph.D. thesis, University of Colorado, Denver, United States (2007).

[14] D. T. Brown, Chapter 8 - mooring systems, in: S. K. CHAKRABARTI (Ed.), Handbook of Offshore Engineering, Elsevier, London, 2005, pp. 663 – 708. doi:https://doi.org/10.1016/B978-0-08-044381-2.50015-1.

[15] J. Jonkman, Definition of the floating system for phase IV of OC3, Tech. Rep. NREL/TP-500-47535, National Renewable Energy Laboratory, Colorado, United States (2010).

[16] A. Robertson, J. Jonkman, M. Masciola, H. Song, A. Goupee, A. Coulling, C. Luan, Definition of the semisubmersible floating system for phase II of OC4 (2014).

[17] C. Luan, Z. Gao, T. Moan, Design and analysis of a braceless steel 5-MW semi-submersible wind turbine, in: Proocedings of the ASME 2016 35th International Conference on Offshore Mechanics and Arctic Engineering, 2016.

[18] J. F. Manwell, J. G. McGowan, A. L. Rogers, Wind Energy Explained: Theory, Design and Application, John Wiley & Sons, Ltd, 2009. doi:10.1002/9781119994367.index.

[19] M. Hansen, Aerodynamics of Wind Turbines, Earthscan, 2013.

[20] J. Vaal, M. L.Hansen, T. Moan, Effect of wind turbine surge motion on rotor thrust and induced velocity, Wind Energy 17 (1) (2014) 105–121. doi:10.1002/we.1562.

[21] M. D. Pedersen, Stabilization of floating wind turbines, Ph.D. thesis, Norwegian University of Science and Technology, Trondheim, Norway (2017).

[22] J. Jonkman, S. Butterfield, W. Musial, G. Scott, Definition of a 5-MW reference wind turbine for offshore system development, Tech. Rep. NREL/TP-500-38060, National Renewable Energy Laboratory, Denver, United States (2009).

[23] F. Nielsen, T. Hanson, B. Skaare, Integrated dynamic analysis of floating offshore wind turbines, in: Proceedings of the 25th International Conference on Offshore Mechanics and Arctic Engineering (OMAE2006), 2006.

[24] T. J. Larsen, T. D. Hanson, A method to avoid negative damped low frequent tower vibrations for a floating, pitch controlled wind turbine, Journal of Physics: Conference Series 75 (7).

[25] J. M. Jonkman, Influence of control on the pitch damping of a floating wind turbine, in: Proceedings of the ASME Wind Energy Symposium, 2008.

[26] C. Luan, V. Chabaud, E. E. Bachynski, Z. Gao, T. Moan, Experimental validation of a time-domain approach for determining sectional loads in a floating wind turbine hull subjected to moderate waves, Energy Procedia 137 (2017) 366 – 381, 14th Deep Sea Offshore Wind R&D Conference, EERA DeepWind'2017. doi:https://doi.org/10.1016/j.egypro.2017.10.361.

[27] SINTEF OCEAN, RIFLEX - Theory manual (2016).

[28] SINTEF OCEAN, SIMO - Theory manual (2016).

[29] J. Jonkman, W. Musial, Offshore code comparison collaboration (OC3) for IEA - task 23 offshore wind technology and deployment (2010).

[30] A. N. Robertson, F. Wendt, J. M. Jonkman, W. Popko, H. Dagher, S. Gueydon, J. Qvist, F. Vittori, J. Azcona, E. Uzunoglu, C. Guedes Soares, R. Harries, A. Yde, C. Galinos, K. Hermans, J. B. de Vaal, P. Bozonnet, L. Bouy, I. Bayati, R. Bergua, J. Galvan, I. Mendikoa, C. B. Sanchez, H. Shin, S. Oh, C. Molins, Y. Debruyne, OC5 project phase II: Validation of global loads of the DeepCwind floating semisubmersible wind turbine, Energy Procedia 137 (2017) 38 – 57, 14th Deep Sea Offshore Wind R&D Conference, EERA DeepWind'2017. doi:https://doi.org/10.1016/j.egypro.2017.10.333.
URL http://www.sciencedirect.com/science/article/pii/S1876610217352931

[31] W. Popko, M. L. Huhn, A. Robertson, J. Jonkman, F. Wendt, K. Müller, M. Kretschmer, F. Vorpahl, T. R. Hagen, C. Galinos, J.-B. L. Dreff, P. Gilbert, B. Auriac, F. N. Víllora, P. Schünemann, I. Bayati, M. Belloli, S. Oh, Y. Totsuka, J. Qvist, E. Bachynski, S. H. Sørum, P. E. Thomassen, H. Shin, F. Vittori, J. Galván, C. Molins, P. Bonnet, T. van der Zee, R. Bergua, K. Wang, P. Fu, J. Cai, Verification of a numerical model of the offshore wind turbine from the alpha ventus wind farm within OC5 phase III, in: Proceedings of the ASME 37th International Conference on Ocean, Offshore and Arctic Engineering (OMAE2018), 2018.

[32] R. Cook, Concepts and applications of finite element analysis, 4th Edition, Wiley, 2001.

[33] WAFO-group, WAFO - A Matlab Toolbox for Analysis of Random Waves and Loads - A Tutorial for version 2017, Math. Stat., Center for Math. Sci., Lund Univ., Lund, Sweden (2017).
URL http://www.maths.lth.se/matstat/wafo

[34] A. Næss, T. Moan, Stochastic Dynamics of Marine Structures, Cambridge University Press, 2013, Cambridge Books Online.
URL http://dx.doi.org/10.1017/CBO9781139021364

[35] O. Faltinsen, Sea Loads on Ships and Offshore Structures, Cambridge Ocean Technology Series, Cambridge University Press, 1993.

[36] P. J. Moriarty, A. C. Hansen, Aerodyn theory manual, Tech. rep., National Renewable Energy Laboratory, Denver, Colorado (2005).

[37] M. Lennie, D. Marten, G. Pechlivanoglou, C. N. Nayeri, C. O. Paschereit, Modern methods for investigating the stability of a pitching floating platform wind turbine, Journal of Physics: Conference Series 753 (8) (2016) 082012.

Appendix A. Parametric aerodynamics model based on Dynamic Vortex Theory

Pedersen [21] devised a convenient model for the aerodynamic thrust and torque, where the interconnected nature of those loads are made evident through the so-defined *circulation function*.

From the Kutta-Joukowsky theorem, the lift force $d\mathbf{f}$ on a line element $d\mathbf{l}$ is given by:

$$d\mathbf{f} = \rho \mathbf{u}_r \times \Gamma d\mathbf{l}\,, \tag{A.1}$$

where Γ is the circulation[8] and $\mathbf{u}_r$ is the relative flow velocity, which in a system of cylindrical coordinates (r, θ, z) fixed to the rotor is given by

$$\mathbf{u}_r(t) = \mathbf{e}_z w(t) - \mathbf{e}_\theta \Omega(t) r\,, \tag{A.2}$$

with w being the airflow and Ω the rotor angular velocity. Under the assumption of purely axial inflow, the normal component of $d\mathbf{f}$ is integrated over each of the blades, leading to the following expression for the circulatory thrust, F_c:

$$F_c(t) = \frac{\rho A N}{2\pi} \Gamma(t) \Omega(t)\,, \tag{A.3}$$

where ρ is the density of the air, A is the rotor swept area and N is the number of blades. Equivalently, the circulatory torque is found by integrating the tangential component of $d\mathbf{f}$ along each blade:

$$Q_c(t) = \frac{\rho A N}{2\pi} \Gamma(t) w(t)\,. \tag{A.4}$$

The author then proceeds with a series of simplifications for the circulation function, with the objective of devising an *engineering model* without significant losses in accuracy. Notably, by approximating Γ as an equivalent airfoil model, and assuming a flat-plate behavior for small angles of incidence, the circulation function $g(\Omega, w, u)$ is defined as:

$$g(\Omega, w, u) = \kappa \left[\cos(u) w - \sin(u) \Omega \ell\right]\,, \tag{A.5}$$

where $\kappa = 2\rho A_p R / 3\lambda_*$, with A_p being the swept area corrected for blade tip losses[9], R the rotor radius, λ_* the tip speed ratio for maximum wind power extraction and ℓ a *length scale* factor. The parameter u is the controlled blade pitch angle, which is non-zero in the above-rated region only. The circulatory thrust and torque can then be rewritten as:

$$F_c = g(\Omega, w, u)\Omega, \quad Q_c = g(\Omega, w, u) w\,. \tag{A.6}$$

Drag may be relevant for the torque and, in a lesser degree, for the thrust. The drag thrust and torque are modelled according to

$$F_d = d_F |w| w, \quad Q_d = -d_Q \Omega^2\,, \tag{A.7}$$

where the coefficients d_F and d_Q are determined in terms of losses in typical wind turbines. The following compact model in matrix form is then proposed:

$$\begin{bmatrix} F \\ Q \end{bmatrix} = \begin{bmatrix} d_F |w| & -g(\Omega, w, u) \\ g(\Omega, w, u) & d_Q \Omega \end{bmatrix} \begin{bmatrix} w \\ -\Omega \end{bmatrix}\,, \tag{A.8}$$

[8] The circulation is defined as the integral of the flow velocity field around any closed path C enclosing the airfoil, $\Gamma = \oint_C \mathbf{u} \cdot d\mathbf{l}'$.

[9] A common method for modelling tip loss effects is by reducing the effective rotor radius, through multiplication by a factor $0 < B < 1$. The corrected radius $R_p = BR$ then results in an effective swept area $A_p = B^2 A$.

where the airflow w is given by Equation (9). Pedersen proposes that the low-frequency dynamics of the inflow, w_i, are driven by

$$\mu R_p \dot{w}_i + |w| w_i = \frac{F_c}{2\rho A_p} \,, \tag{A.9}$$

where $\mu = 8/3\pi$ is a *virtual inertia* parameter.